Acta Crystallographica Section D
**Biological Crystallography**
ISSN 0907-4449

# Structure of the diaminopimelate epimerase DapF from *Mycobacterium tuberculosis*

**Veeraraghavan Usha,[a] Lynn G. Dover,[a]‡ David I. Roper,[b] Klaus Fütterer[a]* and Gurdyal S. Besra[a]***

[a]School of Biosciences, University of Birmingham, Edgbaston, Birmingham B15 2TT, England, and [b]Department of Biological Sciences, University of Warwick, Gibbet Hill Road, Coventry CV4 7AL, England

‡ Present address: Biomedical Sciences, School of Applied Sciences, Northumbria University, Ellison Place, Newcastle upon Tyne NE1 8ST, England.

Correspondence e-mail: k.futterer@bham.ac.uk, g.besra@bham.ac.uk

Received 9 December 2008
Accepted 20 January 2009

**PDB Reference:** DapF, 3fve, r3fvesf.

The *meso* (or D,L) isomer of diaminopimelic acid (DAP), a precursor of L-lysine, is a key component of the pentapeptide linker in bacterial peptidoglycan. While the peptidoglycan incorporated in the highly complex cell wall of the pathogen *Mycobacterium tuberculosis* structurally resembles that of *Escherichia coli*, it is unique in that it can contain penicillin-resistant *meso*-DAP→*meso*-DAP linkages. The interconversion of L,L-DAP and *meso*-DAP is catalysed by the DAP epimerase DapF, a gene product that is essential in *M. tuberculosis*. Here, the crystal structure of the ligand-free form of *M. tuberculosis* DapF (*Mt*DapF) refined to a resolution of 2.6 Å is reported. *Mt*DapF shows small if distinct deviations in secondary structure from the two-domain $\alpha/\beta$-fold of the known structures of *Haemophilus influenzae* DapF and *Bacillus anthracis* DapF, which are in line with its low sequence identity (≤27%) to the former. Modelling the present structure onto that of L,L-aziridino-DAP-bound *H. influenzae* DapF illustrates that a rigid-body movement of domain II and a rearrangement of the B4–A2 loop (residues 80–90) of domain I are likely to accompany the transition from the present inactive form to a catalytically competent enzyme. Despite a highly conserved active-site architecture, the model indicates that stabilization of the DAP backbone occurs in *Mt*DapF through a tyrosine residue that is specific to mycobacterial DAP epimerases.

## 1. Introduction

Tuberculosis (TB) is a leading cause of death among the world's poor and latent infections by the aetiological agent, *Mycobacterium tuberculosis*, are estimated to affect one third of the world population (Dye *et al.*, 1999). Penicillin-class antibiotics are clinically ineffective against the tubercle bacillus, despite the presence of penicillin-sensitive target proteins (Goffin & Ghuysen, 2002) and a peptidoglycan component of the mycobacterial cell wall that structurally resembles that of *Escherichia coli* (Dover *et al.*, 2004; Janczura *et al.*, 1981; Petit *et al.*, 1969; Wietzerbin *et al.*, 1974). Peptidoglycan is composed of linear glycan chains that are cross-linked by pentapeptide linkers (Nanninga, 1998; van Heijenoort, 2001). In Gram-negative organisms the third position in the linker pentapeptide is typically *meso*-diaminopimelic acid (*meso*-DAP or D,L-DAP), which is a precursor of L-lysine (Schleifer & Kandler, 1972). However, mycobacteria incorporate two distinct interpeptide linkages, the common D-Ala→*meso*-DAP linkage during exponential growth and a *meso*-DAP→*meso*-DAP linkage, a penicillin-resistant mode of ligation, upon entering stationary phase (Wietzerbin *et al.*, 1974). Given the ability of *M. tuberculosis* to persist in the host during prolonged periods of latency, this unique structural feature may be a contributing factor to the $\beta$-lactam resistance of mycobacteria (Goffin & Ghuysen, 2002; Wietzerbin *et al.*, 1974). The biosynthesis of


**Figure 1**
Reaction catalysed by DAP epimerase.

**Table 1**
Crystallographic data.

Values in parentheses are for the high-resolution shell.

| | |
|---|---|
| Data collection | |
| Unit-cell parameters (Å) | $a = b = 183.6$, $c = 45.2$ |
| Space group | $P6_522$ |
| Wavelength (Å) | 0.976 |
| Resolution range (Å) | 45.22–2.59 (2.73–2.59) |
| Total reflections | 189833 (26167) |
| Unique reflections | 14430 (2020) |
| $R_{\rm merge}$† (%) | 8.6 (75.8) |
| $\langle I\rangle/\langle\sigma(I)\rangle$ | 23.8 (3.8) |
| Completeness (%) | 99.7 (98.4) |
| Multiplicity | 13.2 (13.0) |
| Refinement | |
| Resolution (Å) | 45–2.6 |
| Reflections in working set/test set | 13619/722 |
| No. of protein atoms | 2003 |
| No. of solvent atoms | 58 |
| Wilson $B$ factor (Å$^2$) | 64.8 |
| Average $B$ factor (Å$^2$) | 56.4 |
| R.m.s.d. $B$ between bonded atoms (Å$^2$) | 1.5 |
| $R_{\rm cryst}/R_{\rm free}$‡ (%) | 22.4/25.4 |
| R.m.s.d. bonds (Å) | 0.009 |
| R.m.s.d. angles (°) | 1.36 |
| Ramachandran plot§ | |
| Favoured (%) | 95.3 |
| Allowed (%) | 99.6 |
| Outliers (%) | 0.4 (1 of 277 residues) |

† $R_{\rm merge} = \sum_{hkl}\sum_i |I_i(hkl) - \langle I(hkl)\rangle|/\sum_{hkl}\sum_i I_i(hkl)$, where $I_i(hkl)$ is an individual intensity measurement and $\langle I(hkl)\rangle$ is the average intensity for all reflections $i$. ‡ $R_{\rm work}$, $R_{\rm free} = \sum |F_{\rm o}| - |F_{\rm c}|/\sum |F_{\rm o}|$, where $F_{\rm o}$ and $F_{\rm c}$ are the observed and calculated structure factors, respectively. $R_{\rm free}$ is calculated on the basis of 5% of reflections not used in the refinement (the test set). § Ramachandran statistics were calculated using *MolProbity* (Davis *et al.*, 2007; http://molprobity.biochem.duke.edu/).

*meso*-DAP involves diaminopimelic acid epimerase (DapF), which catalyses the interconversion of L,L-DAP and *meso*-DAP (Fig. 1) through a 'two-base' mechanism involving a pair of cysteine residues (Antia *et al.*, 1957; Wiseman & Nichols, 1984; Pillai *et al.*, 2006). Support for this model has come from recent high-resolution crystal structures of *Haemophilus influenzae* DapF in complex with the D,L and L,L forms of the inhibitor aziridino-DAP (AziDAP; PDB codes 2gke and 2gkj; Pillai *et al.*, 2006). These structures showed the proximal $\alpha$-carbon of the inhibitor to be clamped between the highly conserved cysteine residues at positions 73 and 216, which is stereochemically compatible with their proposed role in deprotonating and reprotonating the $\alpha$-carbon (Pillai *et al.*, 2006). In contrast, the previously determined structure of the apo form of *H. influenzae* DapF (PDB codes 1bwz and 1gqz; Cirilli *et al.*, 1998; Lloyd *et al.*, 2004) shows the enzyme with the catalytic cleft in an 'open' state and the conserved Cys residues forming a disulfide bridge. The conformation of the recently determined structure of *Bacillus anthracis* apo DapF (PDB code 2otn; Matho *et al.*, 2009) displays the Cys thiols in the reduced form, but its overall conformation resembles that of *H. influenzae* DapF in the ligand-free form.

The *dapF* gene (Rv2726c) has been identified as essential for growth under the conditions of genome-wide transposon-site hybridization studies of *M. tuberculosis* and *M. bovis* bacille Calmette-Guérin (Sassetti *et al.*, 2001, 2003), thus potentially representing a target for inhibitor development. Using a novel codon-optimization strategy, we have recently been able to express *M. tuberculosis* DapF (*Mt*DapF) in milligram quantities and have characterized its enzymology *in vitro* (Usha *et al.*, 2006, 2008). At the amino-acid sequence level, *Mt*DapF shows moderate sequence homology to DapF from *H. influenzae* (24% identity) and *B. anthracis* (27% identity), suggesting the possibility of limited structural divergence from an underlying conserved fold. Here, we report the 2.6 Å crystal structure of the ligand-free form of *Mt*DapF.

## 2. Materials and methods

### 2.1. Protein purification and crystallization

The cloning of *Mt*DapF and heterologous overexpression have been described previously (Usha *et al.*, 2006). For this study, we modified the purification protocol reported in Usha *et al.* (2008). Briefly, cells harvested from 4 l cultures were resuspended in loading buffer (see Usha *et al.*, 2008) and lysed by sonication (277 K). The clear lysates (27 000*g*, 45 min, 277 K) were loaded onto an $Ni^{2+}$-chelated HisTrap high-performance column (1 ml; GE Healthcare) and the protein was eluted with a stepwise imidazole gradient (0–500 m*M*) using 20 m*M* Tris–HCl pH 8.0, 500 m*M* NaCl, 5 m*M* DTT, 10% glycerol. The eluate was dialysed into 10 m*M* Tris–HCl pH 8.0, 10% glycerol and 5 m*M* DTT and concentrated to 20 mg ml$^{-1}$ (Amicon YM-10). Sparse-matrix screens (Molecular Dimensions) and a pipetting robot (Mosquito, TTP Labtech) aided the identification of crystallization conditions in sitting-drop vapour-diffusion experiments (291 K; 100 nl protein plus 100 nl reservoir solution). The initial needle-shaped crystals of *Mt*DapF appeared over 2 *M* $(NH_4)H_2PO_4$, 0.1 *M* Tris–HCl pH 8.5 and grew to 25 µm in diameter under optimized conditions [300 nl protein + 300 nl reservoir solution consisting of 1.9 *M* $(NH_4)H_2PO_4$, 0.1 *M* bis-tris propane pH 9.5, 2.5% glycerol]. Prior to flash-freezing in liquid nitrogen, *Mt*DapF crystals were transferred with a nylon loop into mother liquor with stepwise increasing concentrations of glycerol (to 15% in ∼5% steps).

### 2.2. Structure determination

Diffraction data were recorded on ID29 (ESRF, Grenoble, France; Table 1). The large $R_{\rm merge}$ value in the high-resolution shell is most plausibly explained by high redundancy (13-fold) in combination with primary radiation damage incurred over the course of recording 450 frames of 0.25° oscillation. Plotting $R_{\rm merge}$ against frame number showed a plateau of 8% for frames 1–300, followed by a linear increase to 15% over frames 301–450, a telltale sign of radiation damage. A search model for *Mt*DapF was generated using *CHAINSAW* (Collaborative Computational Project, Number 4, 1994) based on PDB entry 1bwz (Cirilli *et al.*, 1998; 24% identity) and molecular-replacement searches (data range 10–4 Å; one molecule per asymmetric unit) were performed with *Phaser* (McCoy *et al.*, 2007). The translation search unequivocally identified $P6_522$ as the correct space group. Poor initial electron-density maps forced the removal of about 25% of the search model. The missing parts of the structure gradually became visible through rebuilding and intermittent refinement with *Coot* (Emsley & Cowtan, 2004), *O* (Jones *et al.*, 1991) and *REFMAC* (Murshudov *et al.*, 1997). The final model comprises residues 1–289, representing the complete sequence of *Mt*DapF bar two chain breaks (149–153 and 185–186), two glycerol molecules, 38 water molecules and a molecule of DTT. Weak or missing density precluded the building of side chains for residues 61, 65, 85, 142, 146, 181, 183, 208, 223, 224, 228 and 241.

### 2.3. Modelling of the 'closed' form

Following superposition of the refined structure of *Mt*DapF on that of *H. influenzae* DapF (PDB codes 2gke and 2gkj; Pillai *et al.*, 2006) by secondary-structure matching and least-squares refinement, domain II was rotated onto its counterpart in 2gke by secondary-structure matching. Residues 80–90 were manually modelled (using *Coot*) onto the corresponding sequence (66–76) in *H. influenzae* DapF. In order to relieve potential steric clashes, the model was minimized by 200 cycles of conjugate-gradient minimization in *CNS* (Brünger *et al.*, 1998).

## 3. Results and discussion

### 3.1. Structure determination and fold comparison

The structure of *M. tuberculosis* DapF was determined by molecular replacement to 2.6 Å resolution. Apart from two disordered surface loops, the model encompasses the complete sequence of *Mt*DapF (residues 1–289) with an additional residue at the N-terminus belonging to the uncleaved $His_6$ affinity tag. The canonical DAP epimerase fold is preserved in *M. tuberculosis* DapF (Figs. 2*a* and 2*b*). Superimposition of *Mt*DapF with the structures of *B. anthracis* DapF (PDB code 2otn; Matho *et al.*, 2009) and *H. influenzae* DapF (PDB codes 1bwz and 1gqz; Cirilli *et al.*, 1998; Lloyd *et al.*, 2004; Fig. 2*b*) led to root-mean-square deviations of 1.54 Å (2otn; 193 $C^{\alpha}$ pairs) and 1.39 Å (1gqz; 206 $C^{\alpha}$ pairs), respectively. The close match of the *Mt*DapF sequence to those of orthologues from the related species *M. smegmatis* and *Corynebacterium glutamicum* (Supplementary Fig. S1[1]) suggests that this finding extends to the entire suborder *Corynebacterineae*, which share the unusual cell-wall architecture of *M. tuberculosis* as an essential element. The monomeric enzyme folds into two $\alpha/\beta$-domains. Distinct structural similarity between these domains, which are related by a pseudo-twofold symmetry axis, is evident. In each domain a central four-turn $\alpha$-helix (labelled A2, A4) points with its amino-terminus towards the active site, which is situated between the domains. Helices A2 and A4 are surrounded by barrel-like $\beta$-sheets which are joined at the domain interface, in effect resulting in a single $\beta$-sheet that extends across the whole length of the cylinder-shaped molecule. Helices A1 and A3 flank the central cleft on either side, packing against the 'outside' face of the barrel-like $\beta$-sheet.

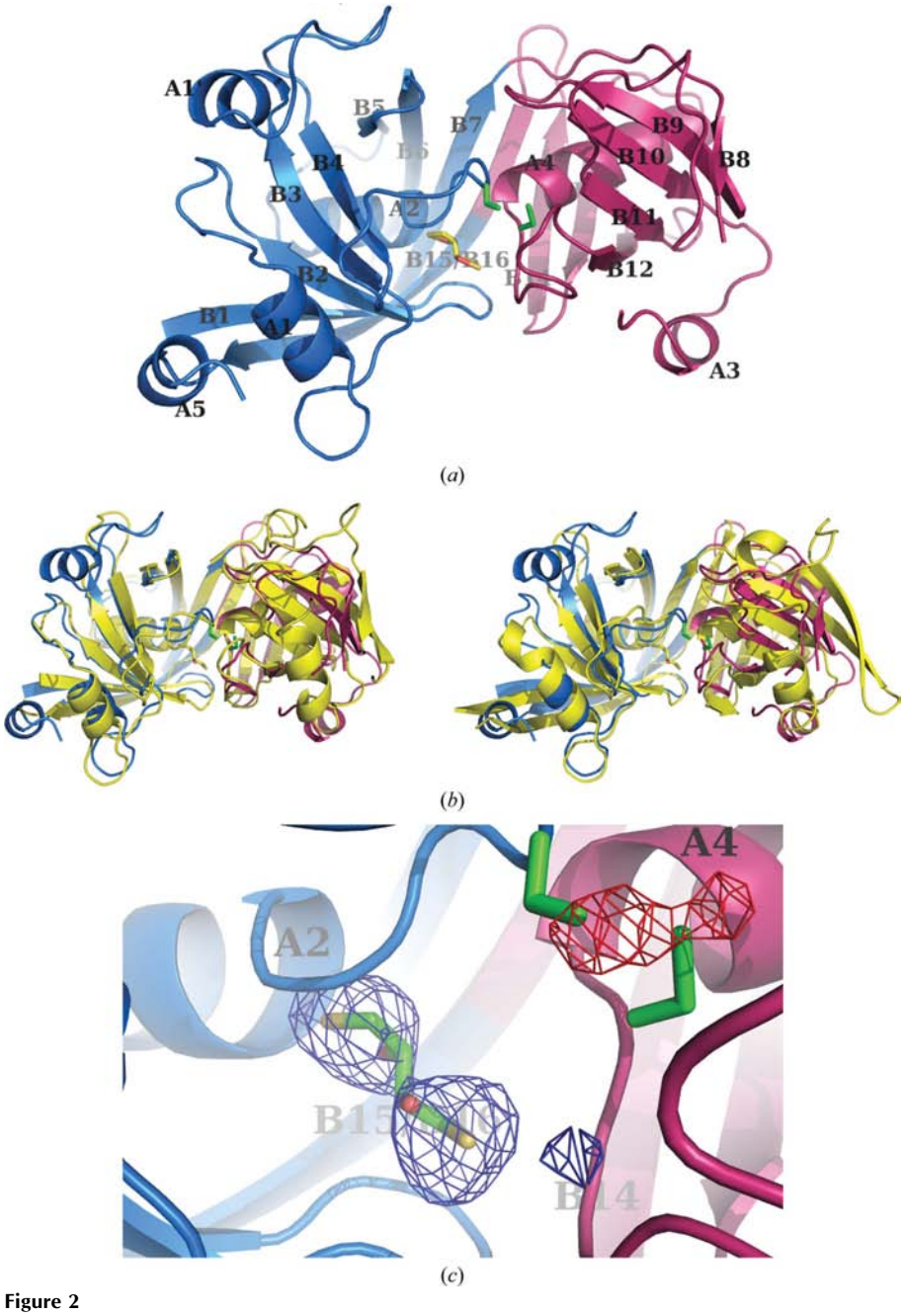


**Figure 2**
Fold of *M. tuberculosis* DapF. (*a*) Ribbon diagram of *Mt*DapF, highlighting the domain structure with domains I and II in blue and red, respectively. Secondary-structure elements are labelled according to the structure of *H. influenzae* DapF (PDB code 1bwz; Cirilli *et al.*, 1998). Strand B15–B16 corresponds to two consecutive strands in *H. influenzae* DapF. The side chains of the active-site Cys residues are shown in green and the bound DTT molecule is shown in yellow sticks. (*b*) Superposition of *Mt*DapF with the previously solved structures of *H. influenzae* DapF (left; PDB code 1bwz) and *B. anthracis* DapF (right; PDB code 2otn). (*c*) Difference Fourier electron-density map contoured at 4$\sigma$ (blue) and −4$\sigma$ (red). The dumbbell-shaped positive density in the active-site cleft was interpreted as a DTT molecule in the reduced state.

Compared with *H. influenzae* DapF, two additional helices appear in *Mt*DapF (Fig. 2*b*): helix A1′ is inserted into the loop linking strands B3 and B4, while helix A5 is appended to the C-terminal strand B15–B16. The latter label reflects the fact that this extended strand, which runs across the domain interface, corresponds to two consecutive strands in *H. influenzae* (and *B. anthracis*) DapF. The loops carrying the active-site cysteine residues are poorly ordered, as manifested by weak density and high atomic displacement factors (supplementary Fig. S2[1]). These loops are known to undergo conformational rearrangements upon substrate binding (see below).

### 3.2. Active site

The active site is located in the prominent cleft between domains I and II. The present structure reflects the catalytically non-productive form of DAP epimerase, characterized by the disulfide bond between the catalytic cysteines (Cys87 and Cys226), the essentiality of which for catalysis has previously been confirmed for *Mt*DapF (Usha *et al.*, 2008). We crystallized *Mt*DapF with 2.5 m*M* dithiothreitol (DTT) present in the crystal drop, incubating trays at 291 K. Nevertheless, the electron density suggests a

[1] Supplementary material has been deposited in the IUCr electronic archive (Reference: HV5124). Services for accessing this material are described at the back of the journal.

mixed state in the crystal. Modelling a disulfide bond between Cys87 and Cys226 led to negative difference density halfway between the $S^{\gamma}$ atoms (Fig. 2*c*), whereas omitting the side chains resulted in distinct positive bridging density indicating the presence of a covalent link. Thus, the observed state is likely to be the net effect of re-oxidation during the course of crystallization (2–3 weeks for the crystals used in this study) and (partial) reduction through primary radiation damage incurred during the X-ray diffraction experiment, to which disulfide bonds are particularly sensitive (Ravelli & McSweeney, 2000).

We observe strong positive difference density (17$\sigma$ above background) adjacent to the N-terminus of helix A2 in the active-site cleft (Fig. 2*c*), a site separated by ∼10 Å from the pair of catalytic cysteines. The density delineates two blobs joined by a thinner neck. When superimposed on the present coordinates, the structure of the C73S mutant of *H. influenzae* DapF (PDB code 2gkj; Pillai *et al.*, 2007) shows a bound tartrate at the site of the density blob. No tartrate was used at any step of the crystal and protein preparations. We tentatively interpreted this density as a DTT molecule, which at full occupancy lowers the $R_{\rm free}$ by a few tenths of one percent but still leaves residual positive density. The presence of an ensemble of different orientations of the DTT molecule may in part explain this unsatisfactory fit.

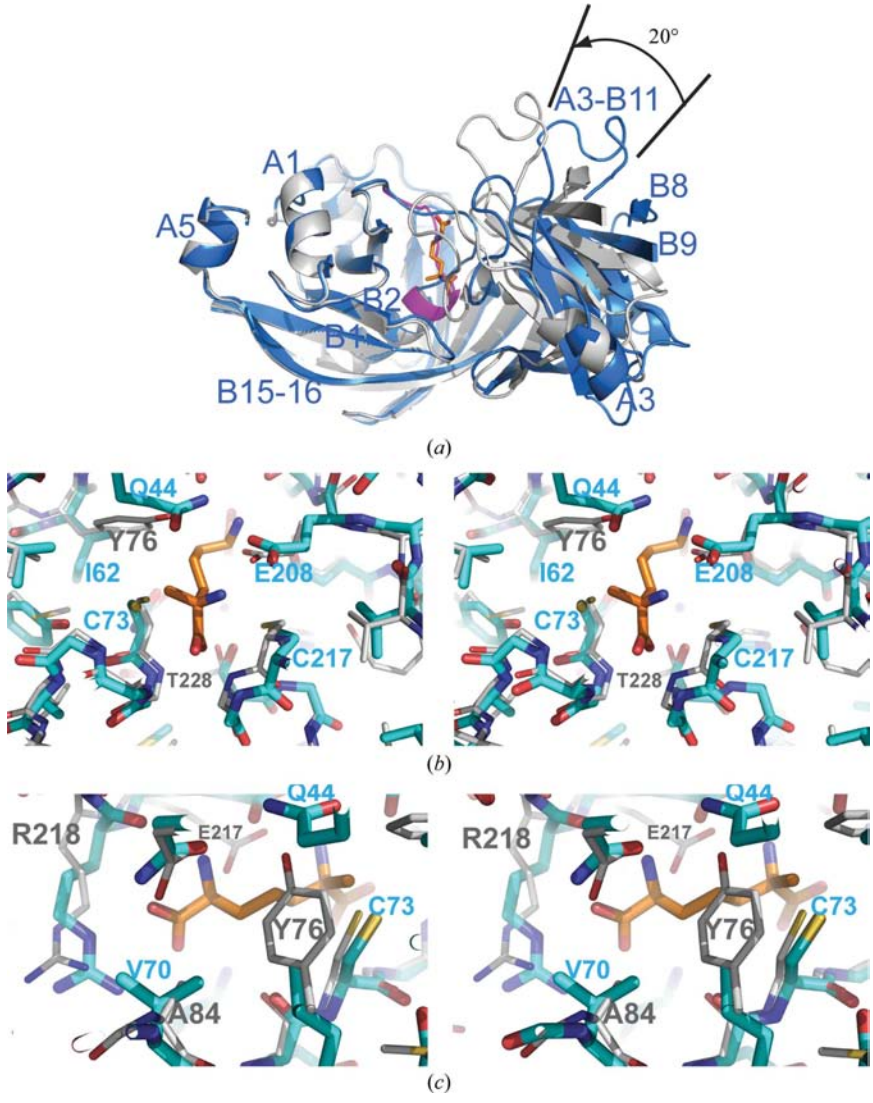


**Figure 3**
Model of the catalytically competent form of *Mt*DapF. (*a*) Ribbon diagram of *Mt*DapF (blue) and a model of its catalytically competent form (grey). A 20° rotation of domain II towards domain I about the viewing direction closes the active site (indicated by a stick model of L,L-AziDAP). Selected secondary-structure elements are labelled for comparison. The B4–A2 loop, modelled according to the structure of L,L-AziDAP-bound *H. influenzae* DapF (PDB code 2gke; Pillai *et al.*, 2006), is shown in magenta. (*b*, *c*) Stereoviews of the active site, centred on the proximal (*b*) and distal (*c*) ends of L,L-AziDAP (orange). Thin grey sticks represent the *Mt*DapF model and light blue thick sticks that of L,L-AziDAP-bound *H. influenzae* DapF (PDB code 2gke). Amino-acid residues referred to in the text are labelled in single-letter code.

### 3.3. A model of the 'closed' form of *Mt*DapF

The present structure displays the enzyme in a catalytically nonproductive state characterized by a disulfide linkage between the active-site Cys residues and the 'open' conformation of the two structural domains (*cf.* Pillai *et al.*, 2006). We investigated what structural changes are required to arrive at the catalytically productive 'closed' state represented by the AziDAP-bound structures of *H. influenzae* DapF (Fig. 3; Pillai *et al.*, 2006). In order to reach this state two separate but interlinked structural changes seem to be required. Firstly, domain II needs to rotate towards domain I about an axis that runs along the central cleft between the domains, oriented approximately perpendicular to the pseudo-twofold axis (Fig. 3*a*). Secondly, for substrate to fit between Cys87 and Cys226, the B4–A2 loop (residues 80–90) in domain I needs to undergo a conformational rearrangement that can be modelled in *Mt*DapF, free of steric clashes, by adopting the geometry of the corresponding residues in AziDAP-bound *H. influenzae* DapF (*Hi*DapF). We note that a rigid-body motion of domain II in conjunction with the aforementioned modelling of the B4–A2 loop in domain I results in an active-site geometry that places all conserved residues required for substrate recognition within hydrogen-bonding or van der Waals contact distance range of the putative substrate-binding site (Figs. 3*b* and 3*c*), highlighting a highly conserved active-site architecture.

Despite a generally high degree of conservation, we observe that Gln44 in *Hi*DapF is substituted by a glycine in *Mt*DapF. Gln44 packs on top of the AziDAP backbone, restricting the substrate's conformational freedom through van der Waals (∼3.6 Å) and hydrogen-bond contacts (Fig. 3*b*). The Gln-to-Gly substitution leaves a void that is taken up by the side chain of Tyr76 (*Mt*DapF), which substitutes for Ile62 (*Hi*DapF; Fig. 3*b*). The substitution of Gln44 by Gly also appears in *B. anthracis* DapF. However, Tyr76 is prevalent in DAP epimerases of the suborder *Corynebacterineae* (Supplementary Fig. S1), a feature that could suggest a route towards the design of a species-restricted inhibitor. Such a DAP epimerase ligand could exploit all conserved contacts in addition to discriminatory interactions with the phenyl ring and the hydroxyl group of Tyr76. This could potentially confer a limited level of species selectivity.

We thank ESRF Grenoble for access to synchrotron beamlines (MX-720) and travel support and Dr Andrew McCarthy for support

during data collection. GSB acknowledges support in the form of a Personal Research Chair from Mr James Bardrick, a Royal Society Wolfson Research Merit Award and as a former Lister Institute-Jenner Research Fellow and from the Medical Research Council.

## References


Antia, M., Hoare, D. S. & Work, E. (1957). *Biochem. J.* **65**, 448–459.

Brünger, A. T., Adams, P. D., Clore, G. M., DeLano, W. L., Gros, P., Grosse-Kunstleve, R. W., Jiang, J.-S., Kuszewski, J., Nilges, M., Pannu, N. S., Read, R. J., Rice, L. M., Simonson, T. & Warren, G. L. (1998). *Acta Cryst.* D**54**, 905–921.

Cirilli, M., Zheng, R., Scapin, G. & Blanchard, J. S. (1998). *Biochemistry*, **37**, 16452–16458.

Collaborative Computational Project, Number 4 (1994). *Acta Cryst.* D**50**, 760–763.

Davis, I. W., Leaver-Fay, A., Chen, V. B., Block, J. N., Kapral, G. J., Wang, X., Murray, L. W., Arendall, W. B. III, Snoeyink, J., Richardson, J. S. & Richardson, D. C. (2007). *Nucleic Acids Res.* **35**, W375–W383.

Dover, L. G., Cerdeno-Tarraga, A. M., Pallen, M. J., Parkhill, J. & Besra, G. S. (2004). *FEMS Microbiol. Rev.* **28**, 225–250.

Dye, C., Scheele, S., Dolin, P., Pathania, V. & Raviglione, M. C. (1999). *JAMA*, **282**, 677–686.

Emsley, P. & Cowtan, K. (2004). *Acta Cryst.* D**60**, 2126–2132.

Goffin, C. & Ghuysen, J. M. (2002). *Microbiol. Mol. Biol. Rev.* **66**, 702–738.

Heijenoort, J. van (2001). *Glycobiology*, **11**, 25R–36R.

Janczura, E., Leyh-Bouille, M., Cocito, C. & Ghuysen, J. M. (1981). *J. Bacteriol.* **145**, 775–779.

Jones, T. A., Zou, J.-Y., Cowan, S. W. & Kjeldgaard, M. (1991). *Acta Cryst.* A**47**, 110–119.

Lloyd, A. J., Huyton, T., Turkenburg, J. & Roper, D. I. (2004). *Acta Cryst.* D**60**, 397–400.

Matho, M., Fukuda, K., Lloyd, A. J., Santelli, E., Jaroszewski, L., Scott, D. J., Liddington, R. C. & Roper, D. I. (2009). Submitted.

McCoy, A. J., Grosse-Kunstleve, R. W., Adams, P. D., Winn, M. D., Storoni, L. C. & Read, R. J. (2007). *J. Appl. Cryst.* **40**, 658–674.

Murshudov, G. N., Vagin, A. A. & Dodson, E. J. (1997). *Acta Cryst.* D**53**, 240–255.

Nanninga, N. (1998). *Microbiol. Mol. Biol. Rev.* **62**, 110–129.

Petit, J. F., Adam, A., Wietzerbin-Falszpan, J., Lederer, E. & Ghuysen, J. M. (1969). *Biochem. Biophys. Res. Commun.* **35**, 478–485.

Pillai, B., Cherney, M., Diaper, C. M., Sutherland, A., Blanchard, J. S., Vederas, J. C. & James, M. N. (2006). *Proc. Natl Acad. Sci. USA*, **103**, 8668–8673.

Pillai, B., Cherney, M., Diaper, C. M., Sutherland, A., Blanchard, J. S., Vederas, J. C. & James, M. N. (2007). *Biochem. Biophys. Res. Commun.* **363**, 547–553.

Ravelli, R. B. & McSweeney, S. M. (2000). *Structure*, **8**, 315–328.

Sassetti, C. M., Boyd, D. H. & Rubin, E. J. (2001). *Proc. Natl Acad. Sci. USA*, **98**, 12712–12717.

Sassetti, C. M., Boyd, D. H. & Rubin, E. J. (2003). *Mol. Microbiol.* **48**, 77–84.

Schleifer, K. H. & Kandler, O. (1972). *Bacteriol. Rev.* **36**, 407–477.

Usha, V., Dover, L. G., Roper, D. L. & Besra, G. S. (2008). *FEMS Microbiol. Lett.* **280**, 57–63.

Usha, V., Dover, L. G., Roper, D. L., Lloyd, A. J. & Besra, G. S. (2006). *FEMS Microbiol. Lett.* **262**, 39–47.

Wietzerbin, J., Das, B. C., Petit, J. F., Lederer, E., Leyh-Bouille, M. & Ghuysen, J. M. (1974). *Biochemistry*, **13**, 3471–3476.

Wiseman, J. S. & Nichols, J. S. (1984). *J. Biol. Chem.* **259**, 8907–8914.